2018

3D Direct Numerical Simulation of Magneto-Caloric regenerators

Ibai Mugica
University of Sherbrooke, Canada, Ibai.Mugica@usherbrooke.ca

Sebastien Poncet
University of Sherbrooke, Canada

Jonathan Bouchard
Laboratoire des Technologies de l'Energie

3D Direct Numerical Simulation of Magneto-Caloric regenerators

Ibai Mugica[1]*, Sebastien Poncet[1], Jonathan Bouchard[2]

[1] Mechanical Engineering Department, Université de Sherbrooke, 2500 boulevard de l'Université, J1K 2R1, Sherbrooke, Canada
* Corresponding Author : i.mugica@usherbrooke.ca

[2] Laboratoire des Technologies de l'Energie (LTE), 600 avenue de la Montagne, G9N 7N5, Shawinigan, Canada

ABSTRACT

Magnetic refrigeration uses magnetic field changes to provoke a phase transition in solid Magneto-Caloric Materials (MCM). Then, using a Heat Transfer Fluid, a Brayton-like refrigeration cycle can be produced. Developing these kind of refrigerators is usually costly, due to the amount of rare earth materials needed for the permanent magnet and the MCM. In order to aid in better designing such machines, a 3D DNS solver was developed. The solver includes the simulation of four different physical phenomena: the magnetic field, fluid velocity field, temperature field, and the Magneto-Caloric Effect. To produce an efficient solver, collateral coupling mechanisms were studied and deemed negligible, including the temperature dependency of the HTF (water) viscosity, and the influence of the magnetic permeability on the internal magnetic field of Gadolinium. The resolution of the physical phenomena was benchmarked separately and then the performance of the cycle solver was compared to a measured prototype. The solutions given by the new 3D DNS solver provide a more accurate description of the temperature field than the 2D solver available in the literature. The authors argue that this is probably partially due to the detailed simulation of the magnetic field (not accounted in 2D codes). The produced numerical solver is aimed to serve as a tool in the design process of magnetic refrigerators. By simulating conceptual magnetic regenerators, it is expected that the new prototypes experience a qualitative jump.

1. INTRODUCTION

Magnetic Refrigeration (MR) is part of the alternative technologies to vapor-compression cycles. Fundamentally, instead of using the latent heat of a liquid-gas phase transition to transport heat from one location to another, MR employs the heat exchange of a ferro-paramagnetic phase transition. This effect was first described by Weiss (1921), and has been referenced later on by the name of Magneto-Caloric Effect (MCE). The MCE of Magneto-Caloric Materials (MCMs) appears near a transition temperature referred as the Curie temperature (T_C). Past this temperature, the MCM falls into a paramagnetic state, where the atomic magnetic moments have increasingly random directions. If an external magnetic field (H_{app}) is applied to the MCM near T_C, the atomic magnetic moments are brought increasingly into an aligned state. Thus, the entropy associated to the magnetic ordering is reduced too, and the excess is translated into an increase of the thermal entropy of the material. Vice versa, when an external magnetic field is retrieved near T_C, the atomic magnetic moments are allowed to return into a more chaotic state, and the MCM cools down if the environment is adiabatic. Magnetization (M) is the macroscopic quantity that describes to which extent are the atomic magnetic moments aligned. M is defined as the resultant magnetic field produced by the atomic magnetic moments of the MCM. Together T, M, and H_{app} from the thermodynamic state variables of the MCM that describe the evolution of MR cycles, much like T, P, and V do for vapor-compression cycles.

One the positive aspects of MR is the quasi-isentropic nature of the magnetic phase change. It has been experimentally shown that 2nd order MCMs like Gadolinium (Gd) show no appreciable hysteresis in single crystals (Dan'kov et al., 1998). This means that future MR systems could develop efficiencies that surpass the current most efficient vapor compression cycles (Yu et al., 2003). The absence of ozone depleting gasses too, makes MR an alternative refrigeration technology that is more aligned with the objectives of the Montreal Protocol. Also, a study hired by the United States DOE (Goetzler et al., 2014) ranked several alternative refrigeration technologies by a criteria of energy savings and development status. MR fell amongst the top 5 technologies that could replace vapor compression cycles.

A drawback of MR technology is the small heat exchange of the most popular MCMs, compared to the moderately high magnetic fields applied to the samples. E.g. Gadolinium (Gd) at its Tc (around 295K) undergoes a maximum adiabatic temperature increase of approximately 5.5K, when the internal magnetic field goes from 0 to 2T (Dan'kov

et al., 1998). Current prototypes circumvent this issue by building Active Magnetic Regenerators (AMR). The solid MCM is set into a porous structure (a regenerator) to exchange heat with a Heat Transfer Fluid (HTF) that will transport the heat from a cold source to a hot sink. Having a porous structure with an increased heat exchange surface reduces the time needed to transfer the heat to the HTF, incrementing the frequency of the refrigeration cycle.

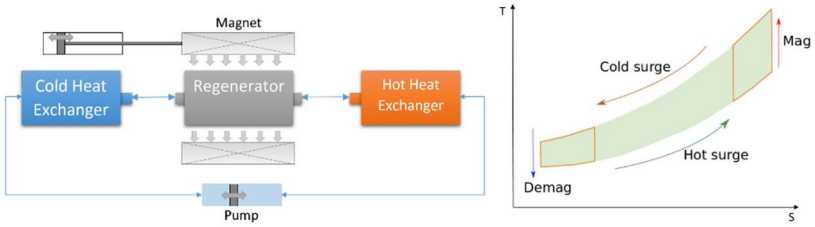

Figure 1: Left, generic setup of an AMR cycle. Right, T-S cycle diagram of a generic AMR cycle. The highlighted cycles represent the end points of the regenerator, and the shaded area would be the collection of all the T-S diagrams.

Then the system is operated in a Brayton-like manner: adiabatic (de)magnetizations of the regenerator change the temperature of the MCM, and then successive HTF surges to evacuate the excess heat to the hot sink or absorb heat from the cold source to warm back again the regenerator. At a steady state, an average temperature gradient is developed between the cold and hot ends of the porous regenerator. This means that every point of the AMR undergoes chained thermodynamic cycle that pumps heat in the direction of the HTF surge. The heat capacity of the MCM stores the heat coming from neighboring cycles depending on how relatively far travels the HTF. So, the MCM acts as a refrigerant and a regenerator at the same time, and thus earning the adjective "active". More modern prototypes rotate a permanent magnet over a series of regenerators with an onset H_{app} of around 1T (Eriksen et al. 2015). This reduces the magnetic forces involved in pushing a magnet into a region with a different M, as there is always another regenerator filling the airgap. Moreover, this setting reduces the variation of torque needed to operate the machine, as the magnet acts like an inertia wheel.

Some practical constrains have hindered the development of MR over decades. One of them is the high capital cost of MCM and permanent magnets, due to their high content of rare earth materials. Nonetheless, some efforts have been made to overcome this drawback. Teyber et al. (2017) presented a methodology to optimize the shape of permanent magnets used in MR to minimize their capital cost. Also, Tan et al. (2013) have found a relevant MCE in $AlFe_2B_2$ alloys, which do not include costly rare earths. On top of the scarcity of rare earths, it is also difficult to manufacture regenerators with fine geometrical structures; and there are few measurements available after the construction of prototypes, due to the relative inaccessibility of the MRs during operation. That is why numerical modelling of AMRs has been present since the early developments of this technology. Numerical models produce information that is valuable to unveil the influence of several design parameters. That way the technological advancements between prototype versions can take bigger leaps over time.

The numerical representation of AMRs gathers the interaction between the hydrodynamic, thermal and magnetic fields, which are coupled by $M = M(T, H)$ and the heat transfer between solid and fluid domains. On top of this, most prototypes present very fine geometric structures that increase the spatial resolution needed to directly simulate all these phenomena. That is why numerical models have usually resorted to many simplification hypotheses to reduce the utilization of computational resources (see Kamran et al. (2016) for a compilation of published numerical codes). To the extent of the authors knowledge, the numerical model presented in this study produces the most detailed results so far amongst the published literature. The solver performs a direct numerical simulation of the involved physical fields on a 3D regenerator geometry. In order to do this, secondary coupling mechanisms were studied to asses their weight on the final solution. These include: the temperature dependency of the viscosity of the Heat Transfer Fluid (water), and the influence of the magnetic permeability on the internal magnetic field of Gd metal.

This paper presents such solver, by validating the resolution of each phenomena separately, and then simulating a published experimental set up. The results are in all cases close to their respective benchmark.

2. Description of the solver

The mathematical model of the AMR solver is composed by the following Partial Differential Equations (PDEs). Fluid continuity and Navier-Stokes equations to calculate the incompressible hydrodynamic field:

$$\nabla \cdot \mathbf{u} = 0 \tag{1}$$

$$\frac{\partial \boldsymbol{u}}{\partial t} + (\boldsymbol{u} \cdot \nabla)\boldsymbol{u} = -\nabla P + \nu_f \nabla^2 \boldsymbol{u} \tag{2}$$

Magneto-Static scalar potential, to calculate the internal magnetic field of the regenerator at every magnet position:

$$\nabla \cdot [\mu_r(T,H)\, \nabla\varphi] = 0 \tag{3}$$

$$\boldsymbol{H} = -\nabla\varphi \tag{4}$$

$$\mu_r = 1 + \frac{M(T,H)}{H} \tag{5}$$

And the energy equations of the fluid and solid domains, to solve the temperature field of the regenerator:

$$c_H(T,H)\frac{\partial T}{\partial t} + \mu_0 T \left.\frac{\partial M(T,H)}{\partial T}\right|_H \frac{\partial H}{\partial t} = \frac{\lambda_s}{\rho_s}\nabla^2 T \tag{6}$$

$$\frac{\partial T}{\partial t} + \boldsymbol{u} \cdot \nabla T = \frac{\lambda_f}{\rho_f c_f}\nabla^2 T \tag{7}$$

The second term of equation (6) represents the heat source (or sink) created by the MCE. If the reader whishes to know more about the thermodynamics of MCMs, is referred to Kitanovski and Egolf (2006), and Roe 2012. This ensemble of PDEs is solved in the OpenFOAM framework. OpenFOAM is a C++ library of Finite Volume Method (FVM) solvers and provides most of the numerical tools needed for any Field Operation And Manipulation (FOAM), with a relatively intuitive syntax. The calculation of $\boldsymbol{u}$, T, and H fields is divided in three different meshes. The mesh to solve the fluid velocity is reused for the solution of the fluid energy equation. To calculate the magnetic field, two meshes are needed: one that represents the non-magnetic surroundings of the regenerator ($\mu_r \approx 1$), and another one for the MCM ($\mu_r = \mu_r(T,H)$). The later is reused to calculate the temperature field of the solid domain. The unstructured meshes are constructed with snappyHexMesh, built mainly by hexahedrons and some polyhedrons too.
The coupled solution of different magnetic domains, and the Conjugated Heat Transfer (CHT) need of a boundary condition that links the information between domains (or meshes in this case). In both cases the necessary condition is the conservation of the flux though the interface (magnetic flux $\boldsymbol{B}$, and heat flux). These can be expressed the following way:

$$\mu_r^I \frac{\partial \varphi_I}{\partial n} = \mu_r^{II} \frac{\partial \varphi_{II}}{\partial n} \tag{8}$$

$$\lambda_I \frac{\partial T_I}{\partial n} = \lambda_{II} \frac{\partial T_{II}}{\partial n} \tag{9}$$

These boundary conditions are mathematically equivalent, and thus they were coded the same way. First, the scalar gradient is discretized by 1st order finite differences with respect to the boundary value:

$$\frac{\partial \varphi}{\partial n} = \frac{\varphi - \varphi_{BC}}{\delta_1} \tag{10}$$

Then from equations (8) and (9) is possible to calculate which should be the new boundary value (φ_{BC}) and update that value at the interface of both domains.

3. Validation of the constituent phenomena

OpenFOAM provides a solver to calculate equations (1) and (2) with the SIMPLE(C) algorithm (simpleFoam). It has been widely employed and validated in the past (see Nigro and Marquez Damian (2010) for an example). So, it is considered to provide realistic velocity field calculations for laminar flow cases, where the only hypotheses are the incompressibility of the fluid and the Newtonian nature of viscosity.
The magneto-static solver was tested for the same benchmark Cingoski and Yamashita (1997) employed. It consists of a rectangular prism with a remanent magnetization of $M_{rem} = 8.7 \cdot 10^5\ A \cdot m^{-1}$, and a relative magnetic

permeability of $\mu_r = 1.07$ (see Figure 2). An analytical solution can be calculated for this case with the Biot-Savart law (see Cingoski and Yamashita (1997) for more information). Figure2 shows that consecutive surface refinements lead to the analytical solution of the problem.

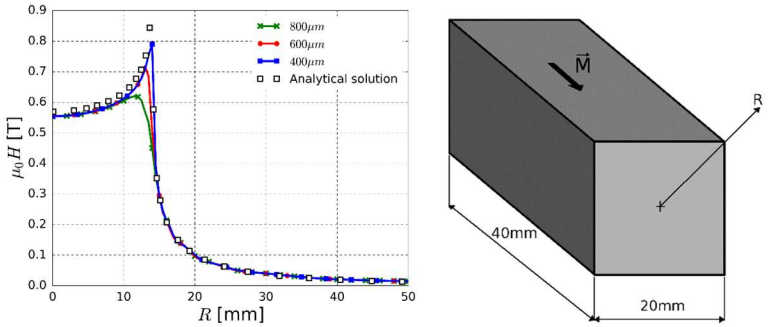

Figure 2: Magnetic field intensity on the surface of the prism. Lines represent the smallest cell sizes on the surface of the magnet. The total size of the meshes are 0.1M, 0.378M, and 5.49M.

The benchmark presented by Ramsak (2015) was replicated to test the present solver for the calculation of a CHT problem. The numerical benchmark consists of a 2D Backwards-Facing Step with a heated slab at the lower wall of the fluid domain (see Figure 3). First the solution (computed by the native solver simpleFoam) of the fluid velocity was compared to the numerical solutions of Kanna and Das (2006). As seen on Figure 3 the fluid profiles match quite closely. The location of the flow detachments at $x_1 = 12.2h$, and the reattachments at $x_2 = 9.7h$ and $x_3 = 20.96h$ were also predicted. Figure 4 shows the Nu and T profiles at the fluid-solid interface for various $k = \lambda_s/\lambda_f$ ratios, after a Grid Sensitivity Analysis (GSA) was done. The employed mesh had square cells uniformly distributed along both domains that had sides $42.86 \cdot 10^{-3}h$ long.

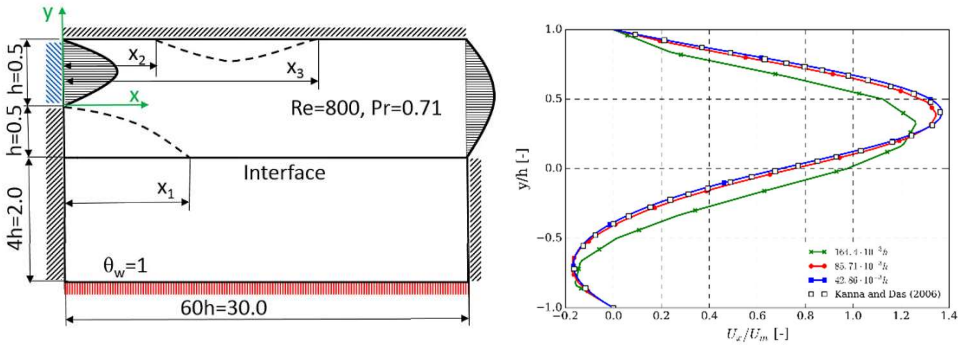

Figure 3: Left, description of the CHT benchmark case (modified schema from Ramsak (2015)). Right, velocity profiles of the BFS at $x = 6h$. Lines represent different cell sizes. Results are compared to the DNS stream function vorticity solution provided by Kanna and Das (2006) in a 151x81 grid.

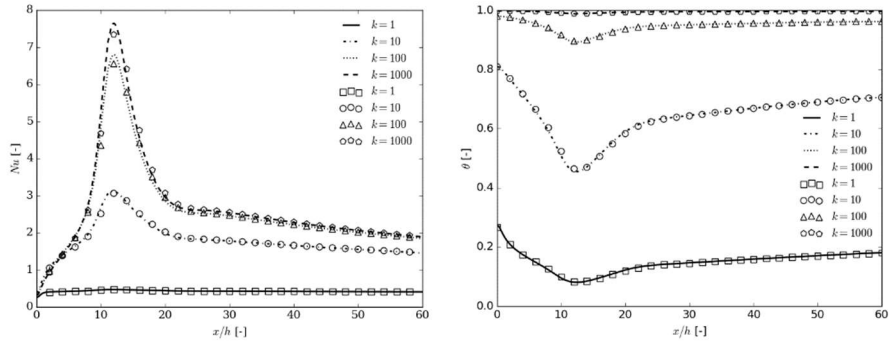

Figure 4: Temperature and Nu profiles at the fluid-solid interface of the benchmark presented in Figure 3. Markers represent data from Ramsak (2015) and lines the solution computed by the present solver.

The implementation of $M(T,H)$ and $c_H(T,H)$ was done by interpolation tables. For the case of this study, the data was collected for Gd metal from Lee (2004) and Risser et al. (2012) respectively. It is possible to generate these data with the Mean Field Theory (MFT) of ferromagnetic materials (Smart, 1966). However, as shown in Figure 5, the hypotheses adopted in MFT produce adiabatic temperature changes that for some materials do not correlate entirely well with the experimental measurements.

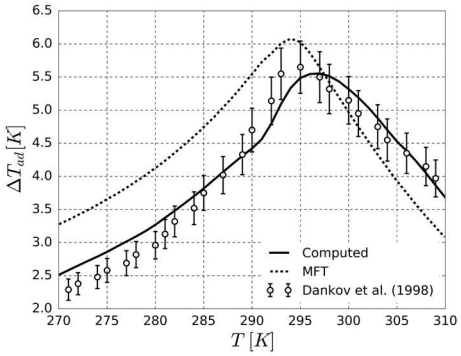

Figure 5: Comparison of the computed MCE, the results of MFT, and experimental data from Dan'kov et al. (1998), for initial temperatures between 270-310K.

4. Secondary coupling mechanisms

The role of the different physical phenomena in AMRs is the following: The magnetic field drives the MCE, and the hydrodynamic field transports the heat of the thermodynamic cycle. The input work is derived from these two fields, and the heat pumped by the system can be calculated with the temperature field solution. Nonetheless there are secondary coupling mechanisms that might influence the coupled solution of the problem.

4.1 Temperature dependence of fluid viscosity

The kinematic viscosity of the HTF (ν_f), can substantially vary within the temperature range of an AMR. In most cases, the HTF employed has a high percentage (more than 80%) of water, whose ν_f varies between 0.8 and $1.785 \cdot 10^{-6}\ m^2 \cdot s^{-1}$ between 0 and 30℃ (Critteden et al. 2012). This means that the Re could double from one place of the regenerator to another, because of the temperature gradient that is present in the AMRs. Changes in Re affect the velocity profile of domains with laminar flow detachment, and thus the convection heat transfer properties (Nu).
In order to check whether this is relevant effect in AMRs, the flow field through a randomly packed-bed of spheres was calculated for different Re. This geometry represents the vast majority of already built MR prototypes. The packed bed was generated following the methodology presented by Boccardo et al. (2015). 8.6mm spheres were packed in an 80mm cylinder to replicate the experiments made by Giese et al. (1998). The trajectories of the particles, and their final positions, were calculated by Newtonian physics for solids, with the help of Blender animation software. Figure 6 shows the close results between the measured and computed radial distributions of porosity. Figure 6 presents the GSA for the case of $Re = 532$ and the comparison of the flow profiles at diminishing Re.

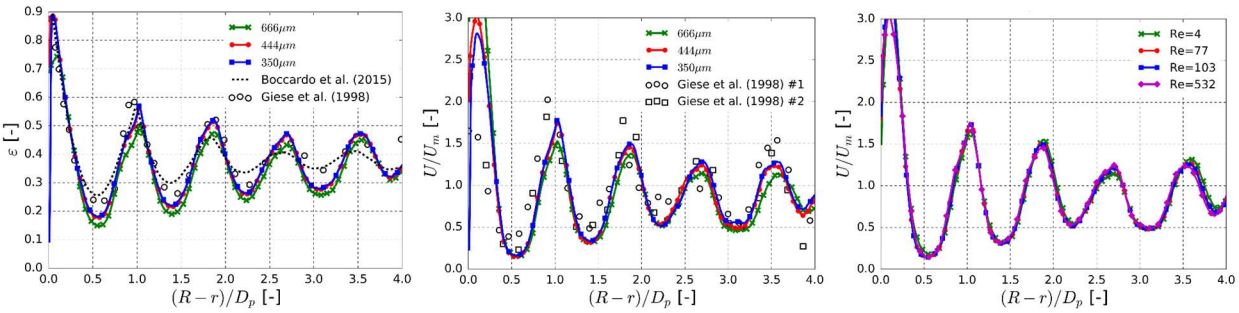

Figure 6: From left to right, 1. Radial distribution of the porosity of the studied randomly packed spheres. 2. Radial distribution of the axial velocity at $Re = 532$, normalized by the mean value. 3. Comparison between the radial distribution of the axial velocity at different Re.

The flow profiles remain more or less unaltered in the studied Re range. Typically, due to the small geometric features of AMRs, the fluid surges have a Re an order or magnitude lower that the most extreme case studied here. This means that the fluid velocity field will not be affected by the temperature field of the AMR, and therefore, the hydrodynamic field can be calculated beforehand, reducing the run time computational load in a significant manner.

4.1 Temperature dependence of MCMs μ_r

Equations (3) and (4) allow the calculation of $\boldsymbol{H}$ through all domains considered. The average H perceived by the MCM though, will differ from H_{app} (measured at the magnet airgap) because of a distinct $\mu_r^{MCM} \neq \mu_r^{air}$ (see Morrish (2001)). The degree by which the average H is reduced (for ferromagnetic materials) from H_{app} depends on the shape of the magnetized sample and μ_r^{MCM}. This relationship can only be analytically calculated for ellipsoids with constant M and is represented by a constant (D):

$$H_{int} = H_{app} - D \cdot M \tag{11}$$

The relationship between the average internal field (H_{int}) and H_{app} can be expressed the following way:

$$\eta = \frac{H_{int}}{H_{app}} = \frac{1}{1 + D(\mu_r - 1)} \tag{12}$$

Figure 7 plots equation (12), and the values of $\mu_r(T, H)$ for Gd metal. From these figures it is not possible to infer whether an average constant value of μ_r could be employed in the numerical calculus of equation (3). Being that the case, the resolution of H would not depend on the temperature field, and like the velocity field, the calculation could be done beforehand, saving computational resources at run time.

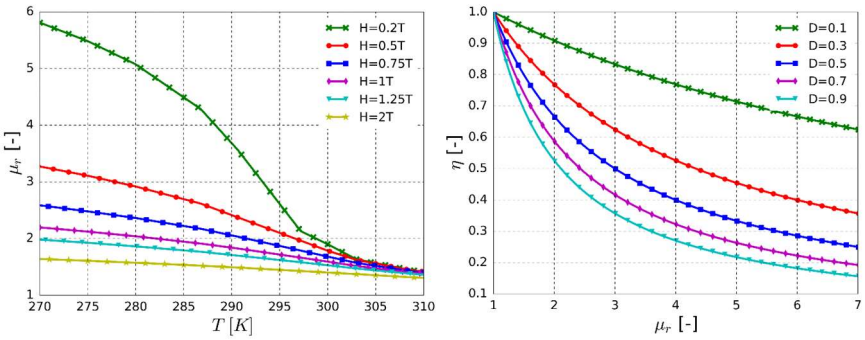

Figure 7: Left, magnetic permeability of Gd metal, calculated from M measurements (Lee, 2004) and equation (5). Right, evolution for the ratio between the internal and applied magnetic field (η), for uniformly magnetized ellipsoids (see equation (12)).

In order to clarify that issue, a single magnetization step was calculated on the full regenerator presented in the next section. It consists of 13 plates 0.9mm thick, 12.5mm wide and 40mm long, separated by 0.8mm thick channels for the HTF (see Figure 8). The magnet held a field of $\mu_0 H = 1T$ at the center of a 40mm airgap and was parallel to the width of the plates. The magnet takes 3s to get to the center of the regenerator from a distance of 130mm. The regenerator was set with a linear temperature gradient ranging from 280 to 310K in the x direction.

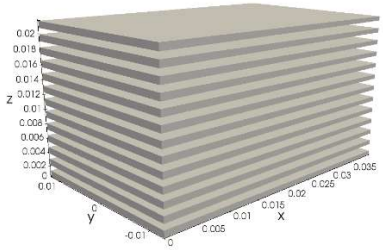

Figure 8: Geometric origin and spatial dimensions of the regenerator constructed by Bahl et al. (2008).

Figure 9 shows the absolute temperature difference between plugging in the $\mu_r(T,H)$ values of Figure 7 and an average $\overline{\mu_r} = 2.1$ calculated between 0-1T and 280-310K. Also, the thermal conductivity of the solid was set to 0, so that the differences between both cases would be most outstanding.

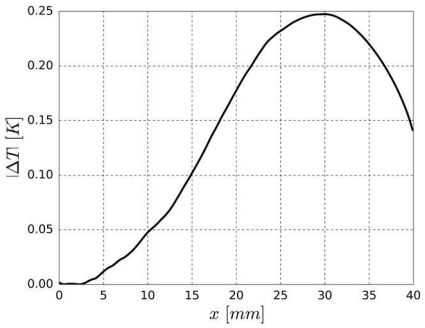

Figure 9: Absolute difference of the temperature profiles (averaged in y and z) between the cases with $\mu_r(T,H)$ and $\overline{\mu_r} = 2.1$, after a magnetization step of the regenerator built by Bahl et al. (2008). The initial temperature gradient was linear along x and went from 280 to 310K.

The maximum difference of Figure 9 is around 0.25K at $x \approx 30mm$. This place corresponds to an initial temperature of 302.5K, where μ_r is closer to 1.5 than 2.1 (see Figure 7). Nevertheless, the maximum difference is less than the expected accuracy from the MCE calculation (see Figure 5), so a constant average $\overline{\mu_r} = 2.1$ will be adopted in the full AMR simulations.

5. Full AMR simulations

The AMR simulated in this section is a replica of the experimental set up of Bahl et al. (2008). First of all, a GSA study was conducted, and it was concluded that the following mesh sizes do not show significant discretization errors:

Domain	Smallest cell size	Number of cells
MCM	66.6μm	2.18M
HTF	27.7μm	1.84M
Non -Magnetic Surroundings	66.6μm	2.57M

Table 1: Final size of the meshes used for the AMR cycle simulation of the regenerator built by Bahl et al. (2008).

The magnetic field of the last subsection was calculated with the same mesh size of the previous Table 1. The cold and hot ends of the regenerator were modelled with perfect heat exchangers. The cold side was set to behave adiabatically (zero load), and the hot end was set at a constant temperature of 300K. Figure 10 shows a clear improvement in the prediction of the temperature span of the regenerator, compared to the 2D code of Petersen et al. (2008).

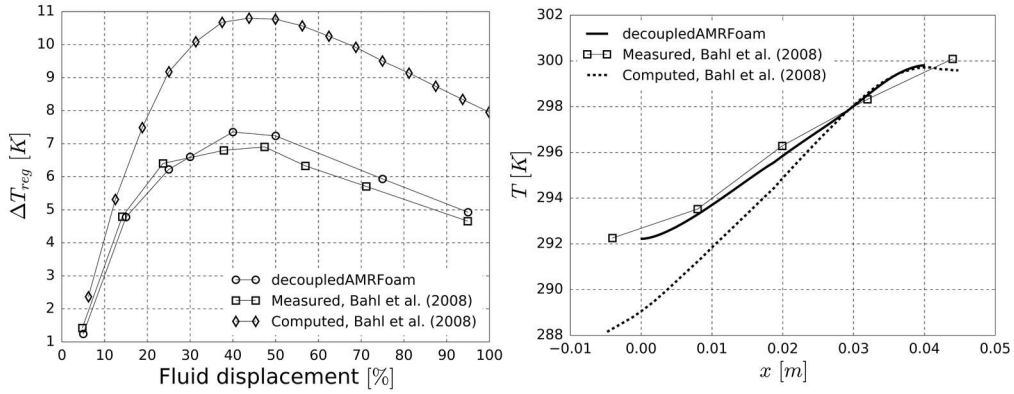

Figure 10: Left, evolution of the temperature span of the plate regenerator built by Bahl et al. (2008), as the fluid displacement of the surges increases. The fluid displacement is relative to the length of the regenerator. Right, temperature profile of the regenerator built by Bahl et al. (2008), at 50% fluid displacement.

The abscissa of Figure 10 (on the left) represents the distance travelled by the fluid surge, relative to the full length of the regenerator. The fluid surge time and the magnetization time were always kept constant (3s). Overall, a 2D simplification of the thermal and hydrodynamic fields of this parallel plate regenerator would not be very far from the 3D case simulated here. However, the magnetic field is set in the transverse direction (y in Figure 8) and Bahl et al. (2008) simplified the magnetization of the solid phase by directly applying a uniform field of 0.97T. After analyzing the results of this 3D solver, it was found that the average internal magnetic field was 0.778T when the regenerator was fully magnetized.

6. Conclusions

A new 3D direct AMR cycle solver has been presented and validated. The validation of the solver was done first by analyzing separately the ability to simulate the constitutive phenomena and then by replicating an experimental AMR set up. In order to reduce the computational resources to a minimum, the weight of the secondary coupling mechanisms was analyzed. Results show that the temperature dependency of the fluid kinematic viscosity of water and the magnetic permeability of Gd metal, do not play an important role on the solution of the full AMR cycle. It was also found that the direct 3D simulation performed substantially better than a former 2D model. It may be attributed to the oversimplification of the action of the magnetic field. On top of those results, this 3D direct AMR solver provides the designer of such prototypes a tool to predict the optimal configuration of the envisioned machine. It constitutes a big leap in AMR codes, because it enables the accurate and efficient simulation of any regenerator geometries.

NOMENCLATURE

$\boldsymbol{B}$	Magnetic flux	(T)
c	Heat capacity	$(J/(K \cdot m^3))$
D	Demagnetization constant	(-)
Gd	Gadolinium	(-)
$\boldsymbol{H}$	Magnetic field intensity	(A/m)
M	Magnetization	(A/m)
$\boldsymbol{n}$	Normal direction	(-)
Nu	Nusselt Number	(-)
P	Pressure	(Pa)
Re	Reynolds number	(-)
t	Time	(s)
T	Temperature	(K)
$\boldsymbol{u}$	Velocity	(m/s)
V	Volume	(m^3)

Greek letters

δ	Distance to the nearest cell	(m)
φ	Magnetic potential	(A)
λ	Thermal conductivity	$(\mathrm{W}/(m \cdot K))$
μ	Magnetic permeability	(N/A^2)
ν	Kinematic viscosity	(m^2/s)
ρ	Density	(kg/m^3)

Subscript

0	Void
app	Applied
C	Curie
f	Fluid
H	Constant magnetic field
int	Interior
r	Relative
rem	Remanent
s	Solid

Acronyms

AMR	Active Magnetic Regenerator
CHT	Conjugated Heat Transfer
DOE	Department Of Energy
FOAM	Field Operation And Manipulation
FVM	Finite Volume Method
GSA	Grid Sensitivity Analysis
HTF	Heat Transfer Fluid
MCE	Magneto-Caloric Effect
MCM	Magneto-Caloric Material
MFT	Mean Field Theory
MR	Magnetic Refrigeration

REFERENCES

Bahl, C. R. H., Petersen, T. F., Pryds, N., Smith, A., (2008). A versatile magnetic refrigeration test device. *Rev. Sci. Instrum.,* 79 (9), 093906.

Boccardo, G., Augier, F., Haroun, Y., Ferr, D., Marchisio, D. L., (2015). Validation of a novel open-source work-flow for the simulation of packed-bed reactors. *Chem. Eng. J.,* 279, 809–820.

Cingoski, V., Yamashita, H., (1997). Modeling of permanent magnets in three-dimensional space using edge finite elements. *J. Appl. Phys.,* 81 (8), 4088–4090.

Crittenden, J. C., Trussell, R. R., Hand, D. W., Howe, K. J., Tchobanoglous, G., (2012). *MWH's Water Treatment: Principles and Design*. New Jersey: Wiley.

Dan'kov, S. Y., Tishin, A. M., Pecharsky, V. K., Gschneidner, K. A., (1998). Magnetic phase transitions and the magnetothermal properties of gadolinium. *Phys. Rev. B,* 57, 3478–3490.

Eriksen, D., Engelbrecht, K., Bahl, C.R.H., Bjork, R., Nielsen, K.K., Insinga, A.R., Pryds, N. (2015). Design and experimental tests of a rotary active magnetic regenerator prototype, *Int. J. Refrigeration*, 58, 14-21.

Giese, M., Rottschfer, K., Vortmeyer, D., (1998). Measured and modeled superficial flow profiles in packed beds with liquid flow. *AIChE J.* 44 (2), 484–490.

Goetzler, W., Zogg, R., Young, J., Johnson, C., (2014). Energy savings potential and RD opportunities for non-vapor-compression HVAC technologies. *Tech. rep., U.S. Department of Energy.*

Kamran, M. S., Sun, J., Tang, Y. B., Chen, Y. G., Wu, J. H., Wang, H. S., (2016). Numerical investigation of room temperature magnetic refrigerator using microchannel regenerators. *Appl. Therm. Eng.,* 102, 1126–1140.

Kanna, R., Das, K., (2006). A short note on the reattachment length for BFS problem. *Int. J. Num. Meth. Fluids*, 50 (6), 683–692.

Kitanovski, A., Egolf, P. W., (2006). Thermodynamics of magnetic refrigeration. *Int. J. Refrigeration,* 29 (1), 3–21.

Lee, J. S., (2004). Evaluation of the magnetocaloric effect from magnetization and heat capacity data. *Physica Status Solidi (b),* 241 (7), 1765–1768.
Morrish, A. H., (2001). *The Physical Principles of Magnetism.* Massachusetts, USA: John Wiley & Sons, Inc.
Nigro, N., Marquez Damian, S., (2010). Comparison of single phase laminar and large eddy simulation (LES) solvers using the OpenFOAM suite. *Asociacion Argentina de Mecanica Computacional XXIX*, 15–18.
Petersen, T. F., Pryds, N., Smith, A., Hattel, J., Schmidt, H., Knudsen, H.-J. H., (2008). Two-dimensional mathematical model of a reciprocating room-temperature active magnetic regenerator. *Int. J. Refrigeration,* 31 (3), 432–443.
Ramsak, M., (2015). Conjugate heat transfer of backward-facing step flow: A benchmark problem revisited. *Int. J. Heat Mass Transf.,* 84, 791–799.
Risser, M., Vasile, C., Keith, B., Engel, T., Muller, C., (2012). Construction of consistent magnetocaloric materials data for modelling magnetic refrigerators. *Int. J. Refrigeration,* 35 (2), 459–467.
Rowe A., (2012). Thermodynamics of active magnetic regenerators: Part I. *Cryogenics* 52 (2–3), 111-118.
Smart, J., (1966). *Effective field theories of magnetism*. Philadelphia: Saunders.
Tan, X., Chai, P., Thompson, C. M., Shatruk, M., (2013). Magnetocaloric effect in AlFe2B2: Toward magnetic refrigerants from earth-abundant elements. *J. Am. Chem. Soc.*, 135 (25), 9553–9557.
Teyber, R., Trevizoli, P., Christiaanse, T., Govindappa, P., Niknia, I., Rowe, A., (2017). Permanent magnet design for magnetic heat pumps using total cost minimization. *J. Magnetism Magnetic Mat.,* 442, 87–96.
Weiss, P., (1921). Le phenomene magneto-calorique. *J. Phys. Radium* 2 (6), 161–182.
Yu, B.F., Gao, Q., Zhang, B., Meng, X.Z., Chen, Z., (2003). Review on research of room temperature magnetic refrigeration. *Int. J. Refrigeration*, 26 (6), 622-636.

ACKNOWLEDGEMENTS

This work is part of the NSERC chair on industrial energy efficiency established at Université de Sherbrooke in 2014 with the support of Hydro-Québec, Ressources Naturelles Canada (CanmetEnergie-Varennes), and Rio Tinto Alcan. The calculations have been performed on the Mammouth Parallèle 2 cluster of Compute Canada, which is also here gratefully acknowledged.